Hindawi
Advances in Civil Engineering
Volume 2022, Article ID 4603007, 17 pages
https://doi.org/10.1155/2022/4603007

Research Article

Experimental Study on the Effect of Large Temperature Difference on Compressive Strength and Pore Structure of Semirigid Base

Ming Dai,[1] Jia Pan,[2] Yanjun Shen,[3] Jianbo Deng,[1] and Yeermulati Muhadeer[1]

[1]*China Railway Construction Xinjiang Jingxin Expressway Co., Urumchi 830000, China*
[2]*College of Architecture and Civil Engineering, Xi'an University of Science and Technology, Xi'an 710054, China*
[3]*College of Geology and Environment, Xi'an University of Science and Technology, Xi'an 710054, China*

Correspondence should be addressed to Yanjun Shen; shenyj@xust.edu.cn

Received 22 January 2022; Revised 17 March 2022; Accepted 24 March 2022; Published 7 June 2022

Academic Editor: Xingxin Chen

Understanding the evolution of mechanical properties and pore structure of semirigid base under large temperature difference is of great significance for evaluating the durability and safety of semirigid base structure and studying the damage cracking mechanism and prevention technology of semirigid base induced by large temperature difference climate. This paper studies the variation law of peak stress and dynamic modulus, the evolution characteristics of pore structure, and the pore size distribution of semirigid base after different cycles at different temperature intervals. Based on the analysis of peak stress and dynamic modulus test results, the degradation effect of freeze-thaw environment (−20°C~20°C) on semirigid base is far greater than that of high-temperature environment (20°C~60°C) and low-temperature environment (−5°C~−30°C). There are significant decreases in peak stress and dynamic modulus of semirigid base in the late cycle (12 to 15 cycles). Under low-temperature and freeze-thaw environments, the axial load resistance of semirigid base is significantly correlated with the deformation resistance, and the correlation between the two is not significant under high-temperature environment. The variability of the thermal expansion and contraction characteristics of the internal microscopic phases of the semirigid base and the force characteristics of the pore interface phases are the root causes of the damage and cracking of the pavement base in a large temperature difference climate.

1. Introduction

Northwest China, influenced by topography, latitude, and altitude factors, formed a more unique and typical temperate continental cold and arid climate; in many areas, the maximum temperature difference between day and night is up to 25~30°C, the maximum annual temperature difference is up to 70~80°C, and the characteristics of the large temperature difference are obvious, so the durability of high-grade highway infrastructure by the large temperature difference appeared to be a significant impact. Semirigid materials, especially cement-stabilized materials, have a strong sensitivity to temperature and humidity due to their structural properties. Under the effect of continuous and periodic high temperature in the summer in the northwest, semirigid base materials inevitably produce drying shrinkage cracking due to changes in humidity and moisture [1,2]. Continuous and cyclic low temperature in winter can easily lead to brittle cracking of semirigid base material [3]. In early spring, the alternating cycle effect of positive and negative temperature is obvious, and the semirigid base material is subject to temperature change and humidity change and produces obvious temperature shrinkage cracking and drying shrinkage cracking [4, 5]. It can be seen that the violent fluctuation of temperature in the area of large temperature difference has a very serious effect on the internal pore cracks of the semirigid base material.

Currently, in the field of road material and pavement design, the main means of monitoring microscopic pore cracks in inorganic solid material are CT techniques [6],

electron microscopy scanning (SEM) techniques [7], digital image correlation (DIC) techniques [8], acoustic emission (AE) techniques [9], and so on. Hu et al. [10] used an X-ray CT device to observe the internal pore space morphology of porous asphalt concrete during their study of the clogging resistance of porous asphalt concrete, thus establishing a link between the pore characteristics and the clogging resistance. Zhao et al. [11] further quantitatively described the proportional pore size and spatial distribution of effective and ineffective pores within porous asphalt concrete. Liang et al. [12] studied the indoor preparation method and field compaction process of cement-stabilized gravel (CSM) material, and the three-dimensional internal structure, pore number, and pore gradation of CSM were studied by industrial CT analysis. SEM techniques have been widely used in recent years for the microstructure characterization of road material and are often combined with X-ray diffraction (XRD) and energy spectrometry (EDS) techniques to characterize the mineral phase changes and elemental distribution of road concrete material [13, 14]. Liu et al. [15] used a combination of SEM and EDS to characterize the pore structure and elemental content of pavement base material mixed with different contents of steel slag (30%, 50%, and 70%), and the results showed that the addition of steel slag significantly improved the frost resistance and dry shrinkage of the pavement base. DIC technology and AE technology have a wide range of applications for the dynamic tracking and quantitative monitoring of the cracking expansion of microcracks throughout the road material [16–18]. However, the application of this technology often requires the use of relevant mechanical tests (three-point bending test and semicircular bending test) to study the mechanism of cracking and expansion of microcracks in the fracture affected area of asphalt concrete [19–21]. However, all of these methods have many limitations, CT technique is costly, SEM is cumbersome and can only be observed locally, DIC technique is based on a macroscopic view of fractures, and AE technique is an indirect study of microporosity through acoustic parameters. Nuclear magnetic resonance (NMR) techniques are fast, accurate, nondestructive, and inexpensive, and most importantly, NMR can quantitatively characterize pore size changes and the number of pores [22]. The cracking of road pavements has been a long-standing problem and has become one of the most serious types of pavement engineering diseases. In recent years, the application of NMR technology in rock, concrete, and even asphalt mixtures has certain significance [22–24]. Menapace et al. [25, 26] used the NMR technique to develop a model between RHI and T_2 values and viscosity as quantitative characterization of asphalt mixture aging. Zhang et al. [27, 28] used 29Si and 27Al MAS-NMR techniques to characterize the amorphous phase Si and the low crystalline phase Al in road-based material, thereby obtaining the degree of polymerization and coordination of silicoaluminate chains. Nicula et al. [29] investigated the freeze-thaw damage condition and porosity magnitude of three blast furnace slag road concrete under a freeze-thaw environment using the NMR technique.

However, in fact, the deterioration mechanism of microcrack pores inside the semirigid base material is often promoted by the mechanical behavior, so the macroscopic mechanical behavior performance must have some inevitable connection with the microfine pore development characteristics; an in-depth study of their relationship can help to reveal the intrinsic cracking mechanism of the material [22–24]. Most focus mainly on the study of thermodynamic parameters and properties of semirigid base material [5,30–35]. Lv et al. [36] found that the strength and frost resistance of cement-stabilized gravel material increase with increasing curing time and cement content through unconfined compressive test, flexural test, and freeze-thaw test studies. Bai et al. [32] investigated the suitability of open-graded cement-stabilized aggregates (OGCSM) produced from recycled aggregates at different replacement rates based on unconfined compressive strength test, indirect tensile strength test, compressive rebound modulus test, dry shrinkage test, frost resistance test, and infiltration test, and the results showed that, with the addition of a certain percentage of recycled aggregates, OGCSM has some potential applications as a base material. However, few studies have dealt with the effects of large temperature differences on the mechanical properties and pore structure deterioration of semirigid base.

This paper combined the local climatic conditions to conduct high-temperature cycle, low-temperature cycle, and freeze-thaw cycle tests on the original samples, respectively. Then, the damage deterioration of the strength and modulus of the semirigid base under the above environmental test conditions was investigated and analyzed by means of the unconfined lateral compressive strength test and dynamic modulus test. Finally, the NMR technique and SEM technique were used to deeply analyze the pore size distribution, pore content, pore structure evolution law with temperature change, and temperature cycle number of semirigid base and finally establish the relationship between strength damage and pore change. The research results of this paper can provide relevant data support and reference to reveal the cracking mechanism of pavement cracks in large temperature difference areas.

2. Materials and Methods

2.1. Materials and Sample Preparation. The samples required for this experiment were obtained by drilling and core sampling of the pavement along the Wumu section of the Jing-Xin Expressway from the Qianshan Interchange (K2 + 690) to the Kusu Interchange (K22 + 027). The specimens were cement-stabilized gravel base material, consisting of 0–5 mm particle size fine aggregate, 5–10 mm particle size coarse aggregate, 10–20 mm particle size coarse aggregate, 20–30 mm particle size coarse aggregate, and P.O42.5 (five) of Portland cement prepared in accordance with 27 : 18 : 34 : 12 (four). The cement comes from Hami Tianshan Cement Co., Ltd. Details of the mineral grade are shown in Table 1, and the physical parameters of raw material are shown in Table 2.

Table 1: Semirigid base mineral grading table.

Sieve hole size		31.5 mm	26.5	19	9.5	4.75	2.36	0.6	0.075
Quality pass percentage (%)		100	—	76.8	46.4	29.3	19.9	9.4	2.7
Target grading range	Upper limit	100	—	86	85	32	28	15	3
	Lower limit	100	—	68	35	22	16	8	0

Table 2: Table of physical parameters of semirigid base.

Binding material dosage (%)	5.0
Maximum dry density (g/cm^3)	2.283
Optimal water content (%)	5.0
Required compaction (%)	98

The original sample in the field needs to be processed for this test as follows: (A) According to the "Highway Engineering Inorganic Binder Stabilized Material Test Specification" (JTGE51-2009), the original sample is cut and polished to the cylindrical sample. (B) Cut part of the cylindrical sample in step 1 into cylindrical sample. (C) Polish and level the cut cylindrical sample to make the upper and lower surfaces smooth and flat. The process is shown in Figure 1.

2.2. Test Methods. The main test steps taken were as follows: (a) The samples were dried and processed by an electric blast dryer, and then the dried samples were soaked in a water tank in combination with the on-site humidity monitoring data until the samples reached the optimum moisture content [32,37,38]. (b) Based on the local climatic and hydrological conditions, this experiment set the temperature intervals as 60~20°C, 20~−20°C, and −5~−30°C, which simulated summer, early spring, and winter environments, respectively, which often constituted a large temperature difference. The temperature environment simulation in summer is 16 hours at a constant temperature of 60°C, and then 8 hours at a constant temperature of 20°C, a total of 24 hours as a cycle. The temperature environment simulation in early spring was -20°C constant temperature for 16 hours and then 20°C constant temperature for 8 hours, a total of 24 hours as a cycle. The temperature environment simulation in winter is −30°C constant temperature for 16 hours, and then −5°C constant temperature for 8 hours, a total of 24 hours as a cycle [4]. Put the soaked sample into the constant temperature and humidity test chamber after wrapping it with cling film. (c) T2 spectral scanning and pore structure analysis of specimens using NMR microstructure analysis system. (d) Measure the longitudinal wave velocity of the specimen using a nonmetallic ultrasonic monitoring analyzer. (e) The uniaxial compression test adopts MTS2000kN universal testing machine, and the loading rate is 1 mm/min. (f) Use a field emission scanning electron microscope to observe the microstructure and pore distribution of the sample after uniaxial compression failure. The detailed test procedure is shown in Figure 1.

3. Results and Discussion

3.1. The Peak Strength and Modulus of Semirigid Base Material. The uniaxial compression test was conducted by an MTS2000 kN universal testing machine produced by Shanghai Jiezhun Instruments Equipment Co., Ltd. The test was carried out in different temperature ranges (20°C~60°C, −20°C~20°C, and −5°C~−30°C) and different cycles on UTM according to "Test Regulations for Stabilizing Material of Inorganic Binders for Highway Engineering" (JTGE51-2009) uniaxial compression test with multiple times (0 times, 3 times, 6 times, 9 times, 12 times, and 15 times), the test loading rate was 1 mm/min, and 3 sets of parallel tests were carried out at each cycle number. The test results are shown in Tables 3–5. The values in the table can be obtained from equation (1):

$$\sigma_c = \frac{4P}{\pi D^2}, \tag{1}$$

where σ_c is the peak stress in the semirigid base material, MPa; P is the maximum pressure when the semirigid base material fails, N; D is the diameter of semirigid base material, mm.

3.2. The Effect of Temperature Interval. The variation pattern of peak stress and difference (the difference of peak stress before and after cycling) of semirigid base material under different temperature intervals is shown in Figure 2(a). As can be seen from the figure, when the number of cycles is small, the peak stress of the semirigid base material is significantly higher in the high-temperature environment (20°C~60°C) than it is in the freeze-thaw environment (−20°C~20°C) and the low-temperature environment (−5°C~−30°C). And when the number of cycles is higher, the peak stress of the semirigid base material is significantly higher in the low-temperature environment than it is in the freeze-thaw environment and the high-temperature environment. It can be seen that the low-temperature environment is more significant for the peak stress deterioration of the semirigid base material in the low cycle region, and the high-temperature environment has a certain improvement effect on the mechanical properties of the semirigid base material. The damage effect of the freeze-thaw environment on the peak stress of semirigid base materials is gradually highlighted in the high-cycle region, and the low-temperature environment has a certain improvement effect on the mechanical properties of semirigid base materials. The magnitude of the peak stress variation in Figure 2(b) is given by equation (2); from Figure 2(b), it can be seen that the mechanical strength of the semirigid base material under freeze-thaw environment shows an overall trend of accelerated deterioration with a deterioration rate of 3.89%/time. The mechanical strength of the semirigid base material under high-temperature environment showed an overall trend of improvement followed by deterioration, the

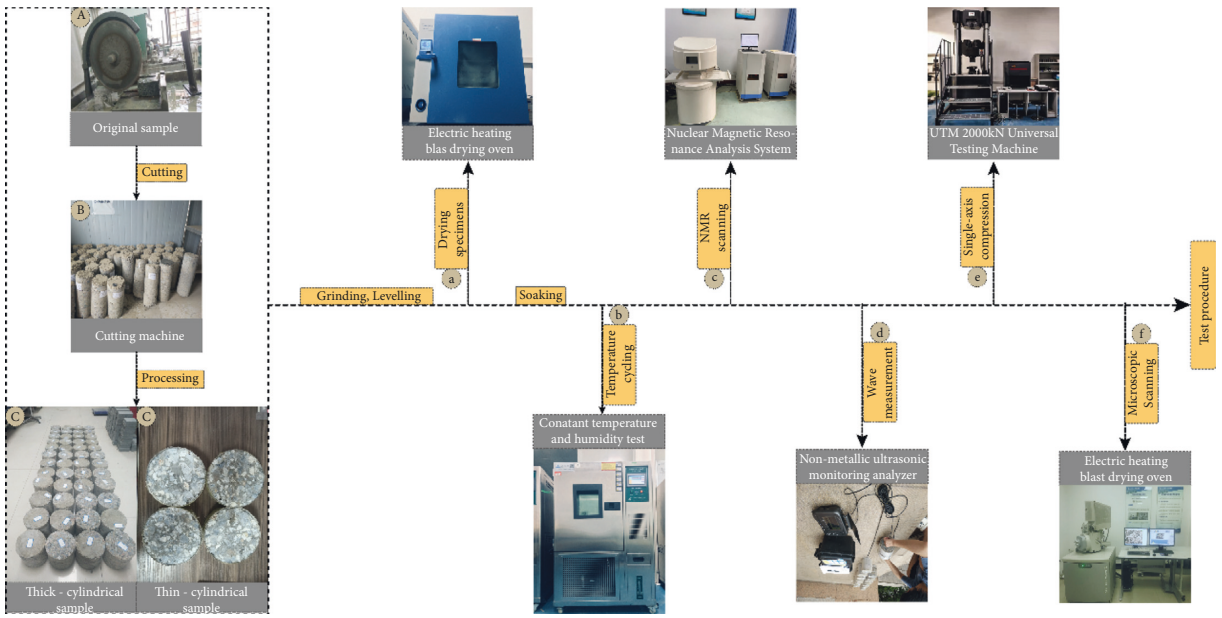

Figure 1: Specimen preparation and test procedure flow.

Table 3: Uniaxial compression experimental results of semirigid base material under the temperature range of 20°C~60°C.

Number of cycles	Parallel strength test value (MPa)			Intensity representative value (MPa)	Standard deviation	Coefficient of variation (%)
0	10.61	12.82	14.06	12.50	1.75	13.95
3	17.43	16.06	15.42	16.3	1.03	6.3
6	12.84	13.15	15.31	13.77	1.35	9.77
9	11.72	13.21	15.63	13.52	1.97	14.6
12	10.88	11.67	13.91	12.15	1.57	12.93
15	11.94	9.55	10.22	10.57	1.23	11.66

Table 4: Uniaxial compression experimental results of semirigid base material under the temperature range of −20°C~20°C.

Number of cycles	Parallel strength test value (Mpa)			Intensity representative value (MPa)	Standard deviation	Coefficient of variation (%)
0	10.61	12.82	14.06	12.50	1.75	13.95
3	11.00	11.50	13.49	12.00	1.32	10.98
6	9.61	12.61	9.79	10.67	1.68	15.77
9	8.61	8.72	8.89	8.74	0.14	1.61
12	7.47	8.21	6.78	7.49	0.72	9.55
15	6.59	5.38	6.53	6.16	0.67	10.93

Table 5: Uniaxial compression experimental results of semirigid base material under the temperature range of −5°C~−30°C.

Number of cycles	Parallel strength test value (MPa)			Intensity representative value (MPa)	Standard deviation	Coefficient of variation (%)
0	10.61	12.82	14.06	12.50	1.75	13.95
3	11.21	9.72	10.13	10.35	1.32	10.98
6	12.37	9.41	12.71	11.50	1.68	15.77
9	12.73	16.00	15.12	14.62	0.14	1.61
12	11.70	14.26	15.61	13.86	0.72	9.55
15	11.69	14.56	14.12	13.46	0.67	10.93

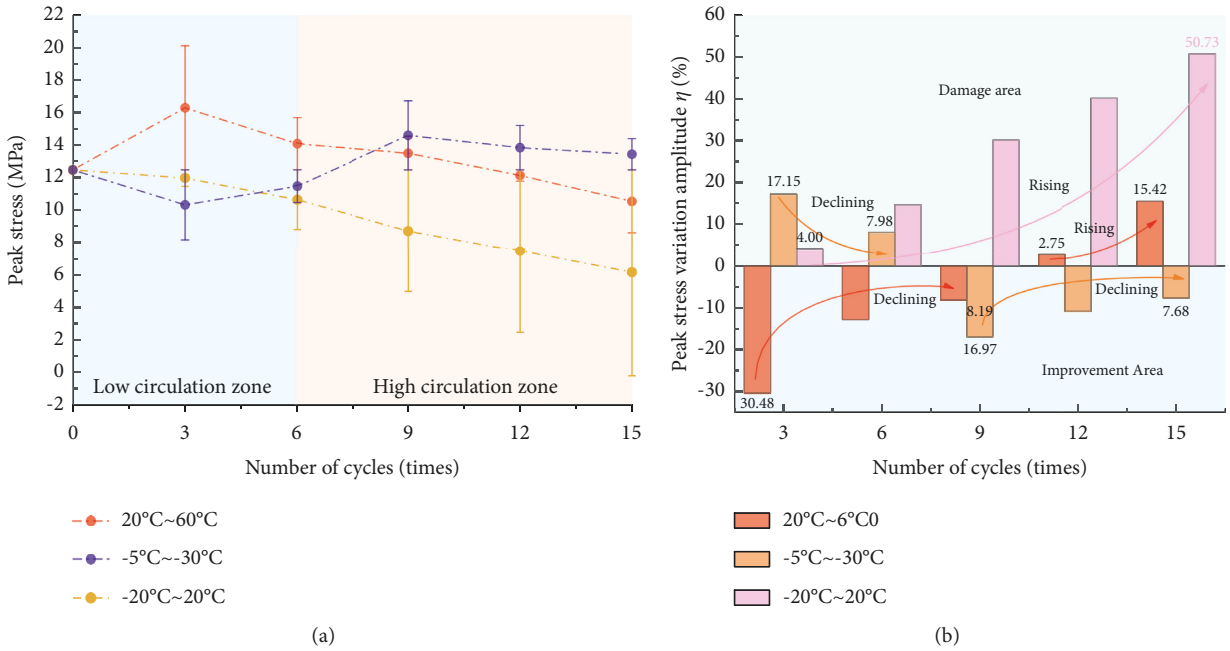

FIGURE 2: Peak strength of semirigid base at different temperature intervals. (a)Variation of peak stress at different temperature intervals. (b) Variation of peak stress at different temperature intervals.

improvement effect gradually weakened, the deterioration effect gradually increased, and the deterioration rate was 4.22%/time. The mechanical strength of semirigid base material under low-temperature environment showed the characteristics of first damage and then improvement, the deterioration effect and improvement effect both gradually weakened, and the deterioration rate was −3.06%/time. It can be seen that the damage effect of freeze-thaw environment on the mechanical properties of semirigid base materials is continuous.

$$\eta = \left[\frac{\left(\sigma_{c,c} - \sigma_{c,t}\right)}{\sigma_{c,c} \times 100}\right], \tag{2}$$

where η is the change in peak stress of semirigid base material before and after cycling, %; $\sigma_{c,c}$ is the peak stress in semirigid base material before cycling, MPa; $\sigma_{c,t}$ is the peak stress of semirigid base material after cycling, MPa.

The longitudinal wave velocity detection of semirigid base materials using MM-A4 nonmetallic ultrasonic monitoring analyzer produced by Beijing Kekangrui Co., Ltd. The link between the dynamic modulus E_D of the semirigid base material and the longitudinal wave velocity V_p is established by (3) [39]. The test results are shown in Tables 6–8.

$$E_D = \left[\frac{\rho V p^2 (1+\mu)(1-2\mu)}{(1-\mu)}\right], \tag{3}$$

where E_D is the dynamic modulus, MPa; ρ is the density of semirigid base material, g/cm^3, and this paper takes $\rho = 2.283$; V_p is the longitudinal wave speed of semirigid base material, m/s; μ is Poisson's ratio of semirigid base material, and this paper takes $\mu = 0.3$.

The variation of dynamic modulus with the number of cycles measured at different temperature intervals is shown in Figure 3. As can be seen from the figure, the overall dynamic modulus value of the semirigid base material in low-temperature environment is low, and the average value can reach 5500 MPa, which is much higher than the modulus value in high-temperature environment (4800 MPa) and freeze-thaw environment (4800 MPa). It can be seen that the semirigid base material has better resistance to deformation in low-temperature environment than in freeze-thaw environment and high-temperature environment. Based on the expectation and standard deviation equation to evaluate the damage factor of dynamic modulus of semirigid base material under different environments (Figure 4(b)), it can be seen that the damage degree of dynamic modulus of semirigid base material under freeze-thaw environment is generally more serious, and the damage impact area is concentrated in 0.67~0.77. The high-temperature environment and low-temperature environment on the dynamic modulus of semirigid base material have a wider range of influence, and the damage impact area is 0.33~0.65 and 0.48~0.66, respectively; thus, it can be seen that the semirigid base material deformation resistance under the action of the periodic freeze-thaw environment is significantly reduced.

3.3. The Influence of the Number of Cycles. The influence of the number of cycles on the peak stress of the semirigid base is shown in Figure 4(a). Under the high-temperature environment, the peak stress of the semirigid base material increased and then decreased with the increase of the number of cycles; the peak stress reached the maximum value of 16.30 MPa after 3 cycles and decreased to the minimum value of 10.57 MPa after 15 cycles, which reduced the stress intensity by 1.5 times.

Table 6: Experimental results of dynamic modulus of semirigid base material under the temperature range of 20°C~60°C.

Number of cycles	Parallel modulus test value (MPa)			Modulus representative value (MPa)	Standard deviation	Coefficient of variation (%)
0	8601	9361	10375	9445	889.91	9.42
3	8693	6440	7520	7551	1126.77	14.92
6	3585	4405	3468	3820	510.55	13.37
9	3165	2841	3468	3158	313.46	9.93
12	4774	4785	6300	5286	877.93	16.61
15	3548	4911	4758	4406	746.86	16.65

Table 7: Experimental results of dynamic modulus of semirigid base material under the temperature range of −5°C~−30°C.

Number of cycles	Parallel modulus test value (MPa)			Modulus representative value (MPa)	Standard deviation	Coefficient of variation (%)
0	11940	13290	12726	12652	678.12	5.36
3	5394	4928	4547	4956	424.18	8.56
6	4312	4367	5167	4616	478.48	10.37
9	8341	7009	8166	7839	723.48	9.23
12	5180	4722	6175	5359	742.88	13.86
15	4819	4132	5267	4739	571.98	12.07

Table 8: Experimental results of dynamic modulus of semirigid base material under the temperature range of −20°C~20°C.

Number of cycles	Parallel modulus test value (MPa)			Modulus representative value (MPa)	Standard deviation	Coefficient of variation (%)
0	17129	16249	18480	17286	1123.68	6.50
3	5483	6142	7250	6292	892.98	14.19
6	4453	4622	5678	4918	663.91	13.50
9	4034	4790	5029	4618	519.85	11.26
12	4834	3928	4333	4365	453.82	10.40
15	3783	3566	4717	4022	611.69	15.21

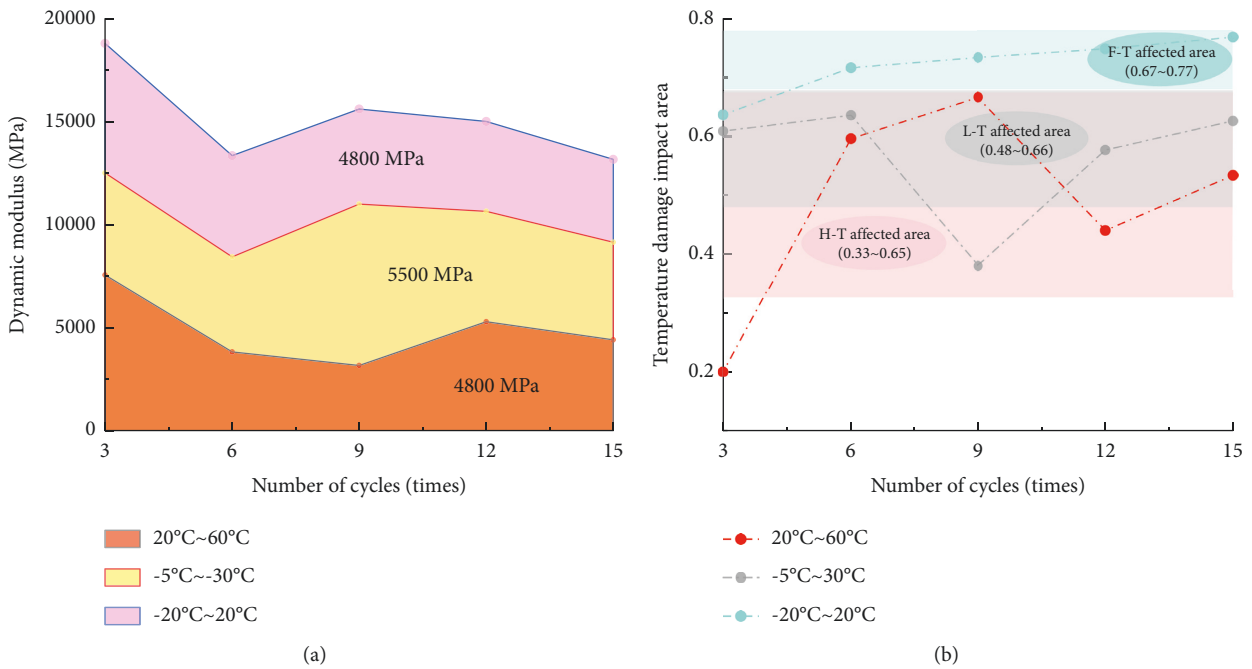

Figure 3: Variation of dynamic modulus of semirigid base material under different temperature intervals. (a) Dynamic modulus stacking diagram at different temperature intervals. (b) Temperature damage impact area.

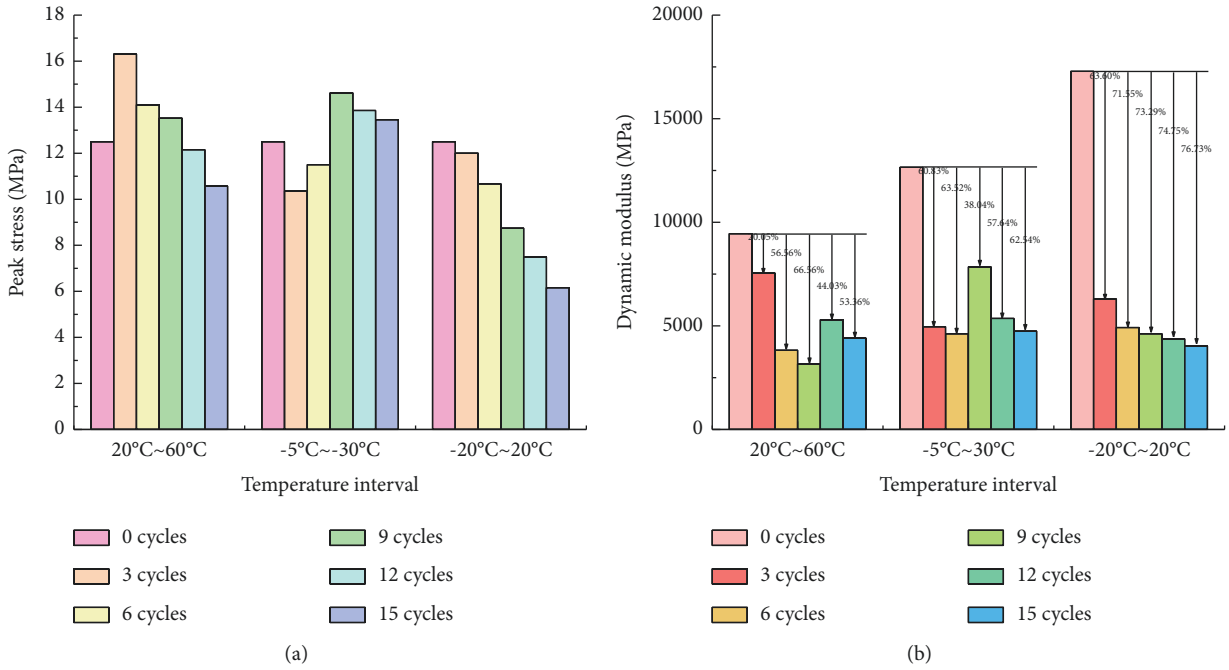

FIGURE 4: Variation of peak stress and dynamic modulus of semirigid base material with the number of cycles. (a) Variation of peak stress with the number of cycles. (b) Variation of dynamic modulus with the number of cycles.

Under the low-temperature environment, the peak stress of semirigid base material decreases and then increases with the increase of the number of cycles, and the peak stress reaches the minimum value of 10.35 MPa after 3 cycles and the maximum value of 14.62 MPa after 9 cycles, which expands the stress intensity by 1.4 times. Under the freeze-thaw environment, the peak stress of the semirigid base material gradually decreased with the increase of the number of cycles, from 12.50 MPa after 0 cycles to 6.16 MPa after 15 cycles, and the stress intensity was reduced by a factor of 2. Accordingly, it can be seen that the number of freeze-thaw cycles has the most significant deterioration effect on the mechanical properties of the semirigid base material.

The influence of the number of cycles on the dynamic modulus of the semirigid base is shown in Figure 4(b). Under the action of high-temperature cycling, the deformation resistance of semirigid base material is very unstable, and the deformation resistance first weakens, then strengthens, and finally weakens with the increase of cycling times. Compared with the dynamic modulus after 0 cycles, the decreases in dynamic modulus after 3 to 15 cycles were 20.05%, 56.56%, 66.56%, 44.03%, and 53.36%, respectively. Under the action of low-temperature cycling, the dynamic modulus of the semirigid base material is basically maintained at about 5500~6000 MPa. Compared with the dynamic modulus after 0 cycles, the decrease of dynamic modulus after 3 to 15 cycles was 60.83%, 63.52%, 38.04%, 57.64%, and 62.54%, respectively. Under the action of freeze-thaw cycling, the damage of the dynamic modulus of the semirigid substrate is very serious; compared with the dynamic modulus after 0 cycles, the decrease of dynamic modulus after 3~15 cycles is 63.60%, 71.55%, 73.29%, 74.75%, and 76.73% respectively.

3.4. Correlation Analysis of Peak Stress and Dynamic Modulus. Based on the above analysis, this paper tries to establish the relationship between peak stress σ_c and dynamic modulus E_D of the semirigid base material by the number of cycles under the effect of large temperature difference so as to analyze the complex characteristics of semirigid base material under large temperature difference [30,35]; its purpose is as follows. First, the later study can predict the elastic-plastic properties or mechanical behavior of the semirigid base material under a large temperature difference environment only by measuring the relevant test parameters [40]. Secondly, it is convenient to analyze and reveal the pore evolution characteristics and damage cracking mechanism of semirigid base material later on [41]. Figures 5(a) to 5(c) show the fitted curves of the peak stress and dynamic modulus of the semirigid base material with the number of cycles at different temperature intervals. The specific fitting equations are shown in Table 9.

Analysis of Figures 5(a) to 5(c) shows that, under high-temperature environment, the resistance to deformation of semirigid base material first decreases and then increases as the mechanical strength decreases. Under freeze-thaw conditions, the resistance to deformation of semirigid base material continues to weaken as the mechanical strength decreases. Under low-temperature environment, the resistance to deformation of the semirigid base material increases with increasing mechanical strength and decreases thereafter with decreasing mechanical strength, but the peaks of both are not at the same number of cycles. Further analysis shows that the peak stress of the semirigid base material shows a certain positive correlation with the dynamic modulus, but this correlation gradually becomes less obvious with the

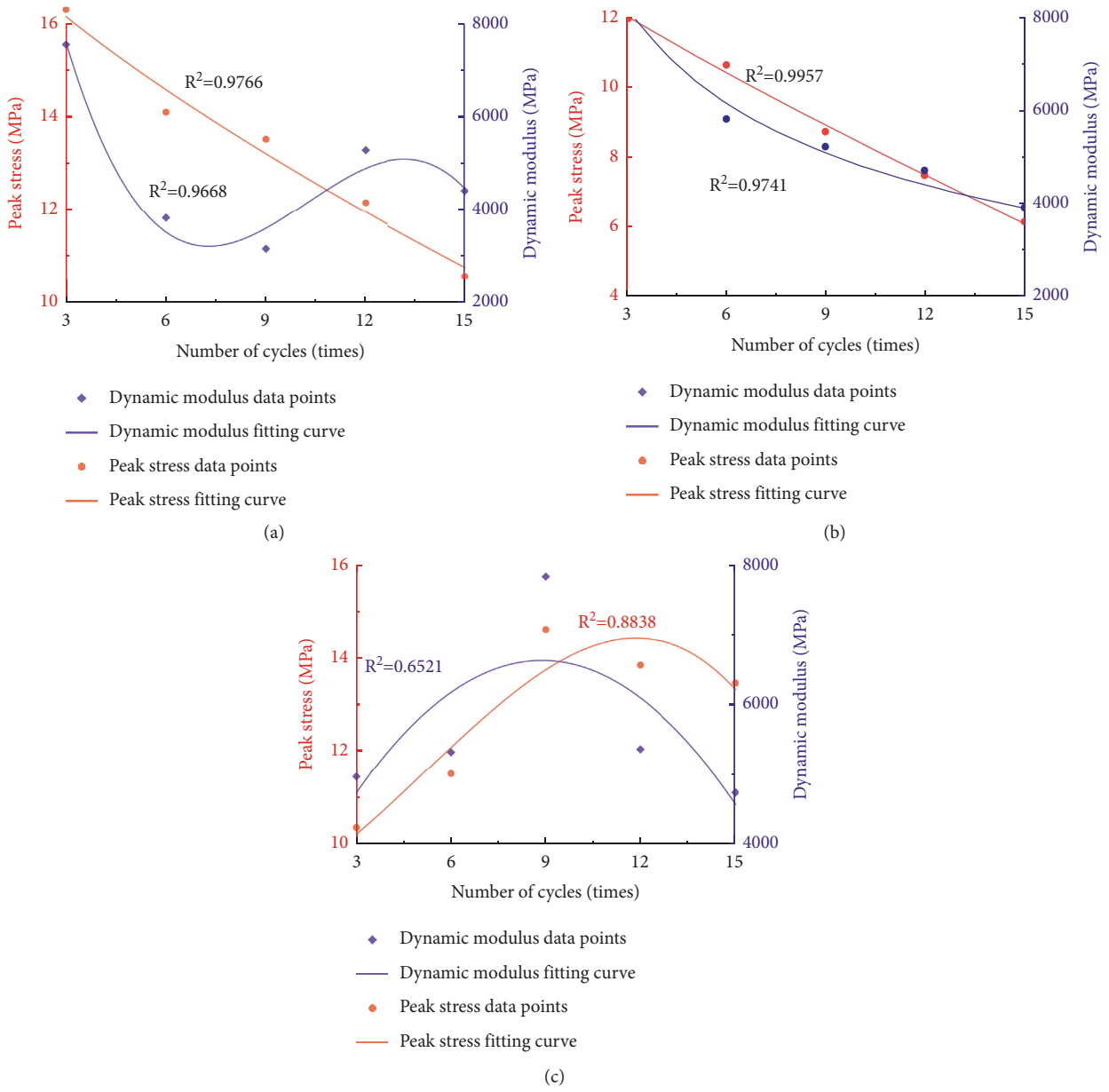

Figure 5: Fitting curves of peak stress and dynamic modulus of semirigid base material versus the number of cycles. (a) Fitting curve at 20°C~60°C. (b) Fitting curve at −20°C~20°C. (c) Fitting curve at −5°C~−30°C.

Table 9: Fitting equations for semirigid base material under different temperature intervals.

Temperature interval	Relationship	Fitting equations
20°C ~60°C	σ_c-N	$\sigma_c = 18.445 - 1.007\,N^{-0.750}$
	E_D-N	$E_D = 18788.943 - 5243.348\,N + 558.736N^2 - 18.192\,N^3$
−20°C ~20°C	σ_c-N	$\sigma_c = 14.053 - 0.771\,N^{0.861}$
	E_D-N	$E_D = 8313.630\,N^{-0.274}$
−5°C ~−30°C	σ_c-N	$\sigma_c = 8.956 + 0.226\,N + 0.097N^2 - 0.005\,N^3$
	E_D-N	$E_D = 2277.745 + 981.578N - 55.255\,N^2$

increase of the number of cycles, indicating that the semirigid base material is not significantly correlated with the axial deformation resistance and load resistance under high-temperature environment, which may be caused by the inhomogeneity of the semirigid base material. Under the freeze-thaw environment, the peak stresses of the semirigid base material showed a linear positive correlation with the dynamic modulus, indicating a significant correlation

between the axial deformation resistance and load resistance of the semirigid base material under the freeze-thaw environment. Under the low-temperature environment, the peak stress of the semirigid base material and the dynamic modulus show a linear positive correlation, which shows that the semirigid base material has a certain significant correlation in the axial antideformation ability and the antiload ability under the low-temperature environment.

3.5. Analysis of Breakage Patterns and Microscopic Damage Characteristics. Figure 6 shows the compression damage patterns of the semirigid base specimens after different number of cycles at different temperature intervals. According to this figure, it can be seen that, under the high-temperature environment, the semirigid base material is damaged with cracks all around, and the cracks produced are mainly vertical cracks, indicating that the semirigid base material is damaged by tension along the interface phase between the aggregate particles and the cement matrix. There is a peeling phenomenon on the surface, and it becomes more and more obvious as the number of cycles increases. Under low-temperature environment, the damage of the semirigid base material is covered with vertical strip cracks around the circumference, which indicates that the semirigid base material produces tension failure along the interfacial phase around the aggregate particles. There is a peeling phenomenon on the surface, and the peeling phenomenon is most serious when it is cycled 6 times to 9 times. Under the freeze-thaw environment, the semirigid base material is covered with cracks around the circumference of the damage, the cracks produced are mainly vertical cracks, and other secondary crack angles are between 0° and 15°, indicating that the semirigid base material produces mixed tensile-shear failure. The scale of surface material shedding increases with the number of cycles. It is easy to see that the damage characteristics of semirigid subgrade materials under different environmental conditions are significantly different, but the damage mode is mainly the tensile damage of the weak interface phase.

The spatial variation and damage evolution of the internal pore structure of the material seriously restrict the macroscopic mechanical properties of the material. In order to better recognize the internal spatial damage condition of the semirigid base material after uniaxial compression under the condition of large temperature difference, SEM tests were conducted on the semirigid material damaged by compression after 12 cycles under different environments, as shown in Figure 7. When the SEM is magnified 5000 times, it can be seen that the drying shrinkage caused by the evaporation of water at high temperature leads to a few through cracks on the surface of the cement matrix, and the through cracks lead to the reduction of the material strength, as can be well demonstrated in Figure 4(a). And a large amount of flocculated C-S-H (calcium silicate hydrate) is produced on the material surface under low-temperature environment, which effectively fills the material microporous cracks and increases the material denseness to some extent, which is consistent with the analysis in Figure 4(a). Under the freeze-thaw environment, the material is affected by the freezing and swelling force generated by the action of the water-ice phase and the contraction force induced by the temperature change together to produce a large number of cracked pores, and the increase of the pore content will inevitably lead to the loss of its bearing capacity, which well explains the deterioration of the peak stress under the freeze-thaw environment in Figure 4(a).

Based on the above analysis, it can be seen that, under the condition of large temperature difference, the semirigid base material is subject to different degrees of rupture damage caused by the drying shrinkage stress induced by water evaporation, the low-temperature shrinkage force induced by temperature reduction, and the freeze-swelling force caused by repeated freezing and thawing, and the degree of damage is affected by the number of cycles and shows significant variability. This damage variability is visualized in the ups and downs of macroscopic mechanical properties (strength and modulus) and fluctuations. Quantitative analysis of the correlation between peak stress and microscopic pore structure and pore size is of great importance to reveal the damage evolution mechanism of semirigid base material under large temperature difference environment. The NMR technique was used to measure the NMR signal intensity of semirigid base material under different environments and after different number of cycles; according to (4) [24,42], the relationship between material pore radius and T_2 transverse relaxation time is established, as shown in Figures 8 and 9. According to the research results of Zhang et al. [23,43], the internal pores of the semirigid base material can be classified into the following four classes, as shown in Table 10.

$$\gamma = \rho_2 F_s T_2, \tag{4}$$

where γ is the pore radius of semirigid base material, nm; ρ_2 is the transverse relaxation strength of semirigid base material, μm/ms, and this paper takes $\rho_2 = 0.003$; F_s is the shape geometry factor, and this paper takes $F_s = 3$; T_2 is the transverse relaxation time of semirigid base material, ms.

According to the analysis of Figures 8 and 9, it can be seen that the lateral relaxation time T_2 distribution curve contains 3~4 peaks, which correspond to less harmful pores, harmful pores, and more harmful pores from left to right. The specific analysis is as follows.

Under the high-temperature environment, the area enclosed by the left peak is the largest, indicating that the number of harmful pores accounted for a large proportion of the material. At the beginning of the cycle (0 to 3 times), the right peak and the middle peak area appeared to decrease, and then the right peak area and the middle peak area gradually increased with the increase of the cycle times, indicating that the number of harmful pores and multiple harmful pores of the semirigid base material first decreased and then gradually increased. The reason is that, under the action of high-temperature cycle in the early stage, semirigid base material aggregate particles by thermal expansion make the material primary cracks gradually closed, and at this time, the material internal water evaporation effect is not significant, so as to enhance the bond between the aggregate

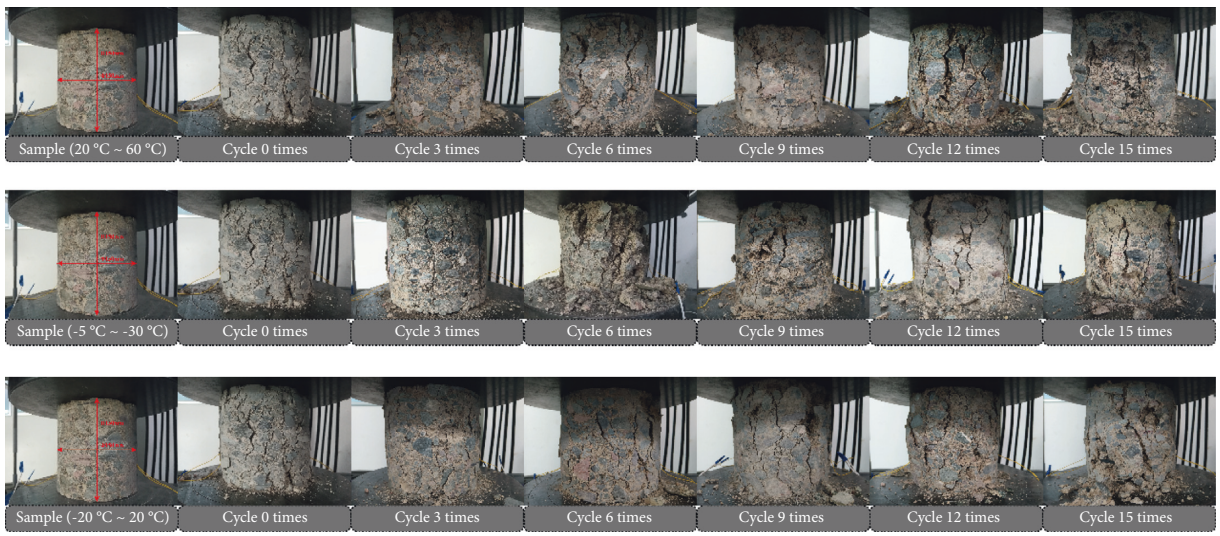

Figure 6: Failure modes at different temperature intervals and number of cycles.

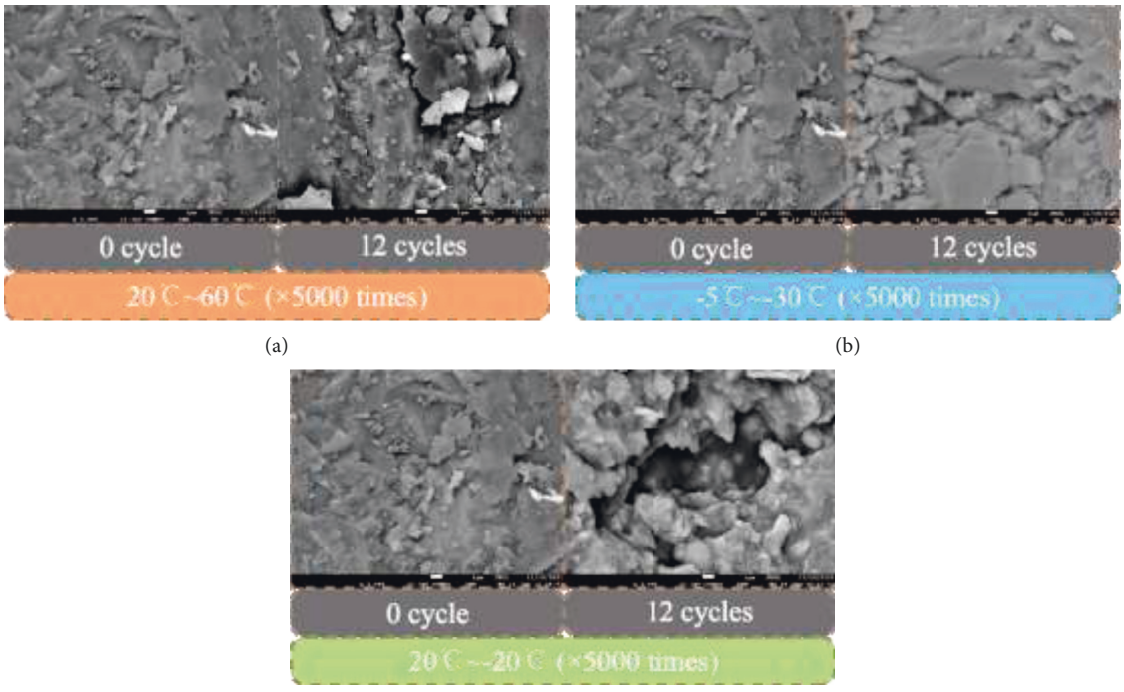

Figure 7: SEM images of specimens damaged by compression after 12 cycles at different temperature intervals. (a) 20°C~60°C (×5000 times). (b) −5°C~−30°C (×5000 times). (c) 20°C~−20°C (×5000 times).

and cement matrix and improve the mechanical strength of the material semirigid base material; with the increase of the number of cycles and cycle time, the excessive expansion thermal stress and the temperature stress generated by the evaporation of a large amount of water make the concrete aggregate particles between the extrusion breakage and cement matrix shrinkage cracking, thus producing a large number of harmful pores and multiharmful pores, which eventually lead to the reduction of mechanical strength of semirigid base materials [44].

Under the low-temperature environment, the sum of the area occupied by each peak gradually decreases with the increase of the number of cycles, indicating that the number of pores of the material as a whole becomes a decreasing trend. At the beginning of the cycle (3~6 times), the area occupied by the right and middle peaks was the largest and then decreased with the increase of the cycle number, indicating that the mechanical strength of the semirigid base material was seriously damaged at the beginning of the cycle and then slowly rebounded with the cycle number. The precooling shrinkage of the aggregate

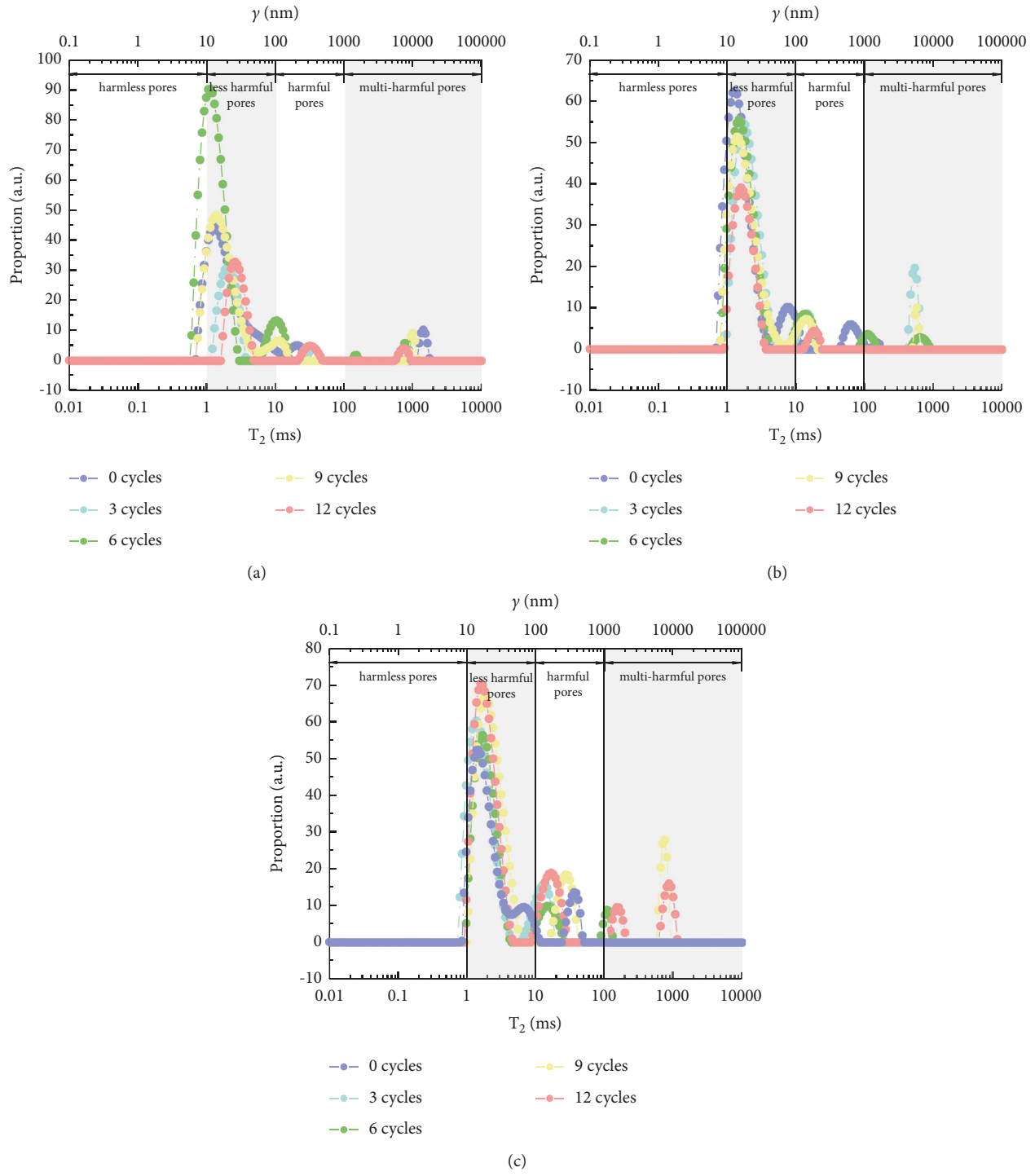

Figure 8: Pore distribution characteristics of semirigid base material after different cycles at different temperature intervals. (a) 20°C~60°C. (b) −5°C~−30°C. (c) 20°C~−20°C.

inside the semirigid base material at the early stage of the low-temperature cycle makes the cracks near the interface phase gradually expand; while the pore water is affected by the low temperature to produce water-ice phase change, volume expansion leads to the pore wall extrusion breakage, resulting in a significant reduction in strength compared to room temperature; as the low-temperature cycle continues, the pore water-ice phase change completely fills the internal pores of the material, so that it forms an "organic whole" with the semirigid base; in addition, the continuous low-temperature cycle leads to a reduction in the difference between the contraction characteristics of each microphase inside the semirigid base, which eventually leads to an increase in the strength of the semirigid base material [45].

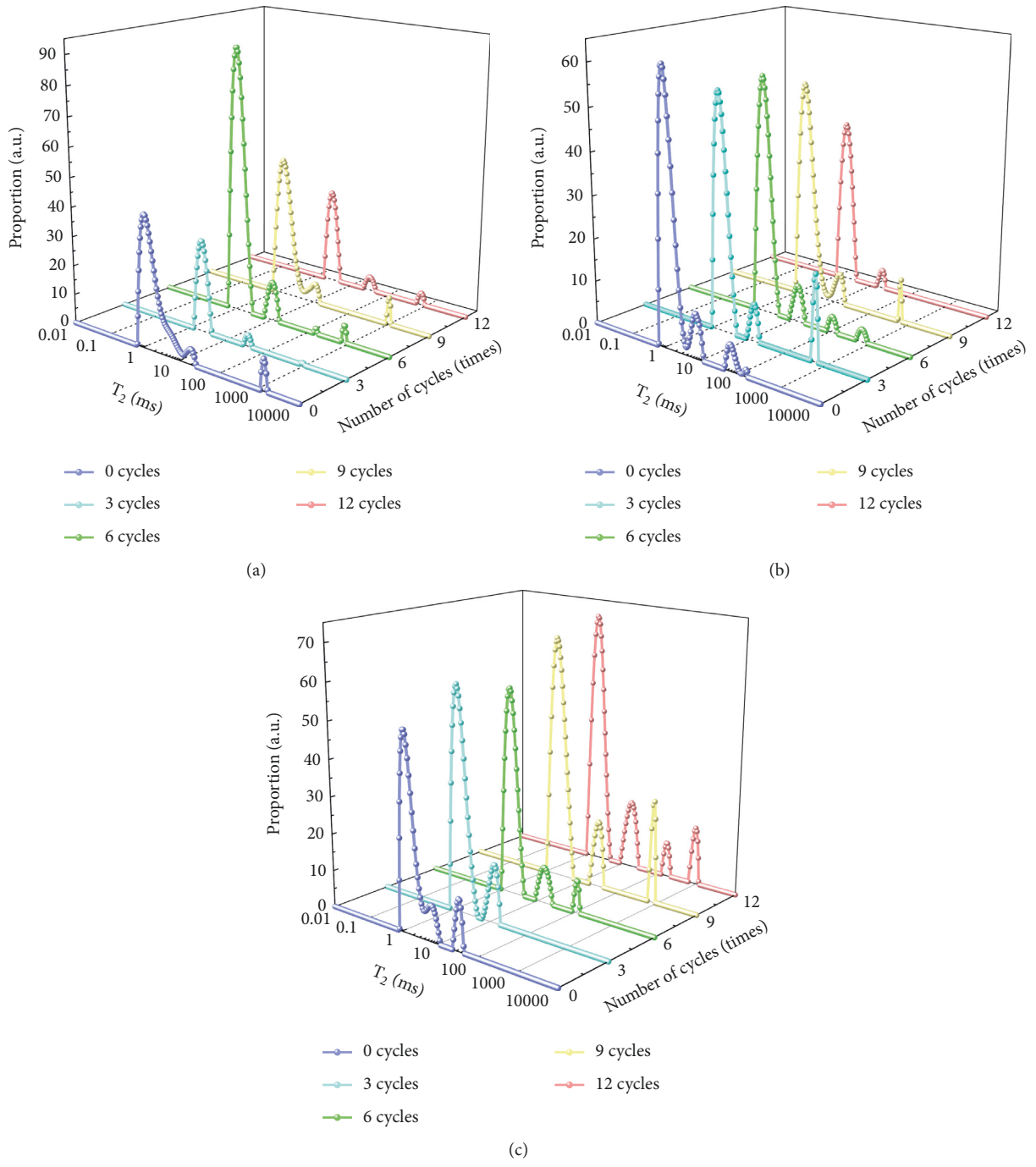

Figure 9: Pore distribution characteristics of semirigid base material after different cycles at different temperature intervals (3D). (a) 20°C~60°C. (b) −5°C~−30°C. (c) 20°C~−20°C.

Under the freeze-thaw environment, the area occupied by each peak shows an increasing trend with the increase of the number of cycles, among which the number of harmful pores and the number of multiharmful pores increase more obviously, which shows that the freeze-thaw cycle has a more significant effect on the change of pore results of the semirigid base material. As a temperature-sensitive material, the semirigid base is particularly sensitive to the freeze-thaw environment, which can be seen from the above analysis. The pore water in the material produces frost heaving stress superposition on the pores under the repeated action of "freeze-thaw," the thermal expansion and cold contraction characteristics of each microscopic phase are significantly different under the repeated action of "freezing-thawing," which easily produces shrinkage stress superposition on the interface phase, and the large increase of harmful pores leads to significant deterioration of mechanical strength of the base material [46].

The area distribution of T_2 spectrum is proportional to the decay of free water inside the pores of different pore

Table 10: Pore grade classification (Liu et al. and Zhang et al.) [23, 43].

Pore category	Harmless pores	Less harmful pores	Harmful pores	Multiple harmful pores
Aperture size	<10 nm	10 nm~100 nm	100 nm~1000 nm	>1000 nm

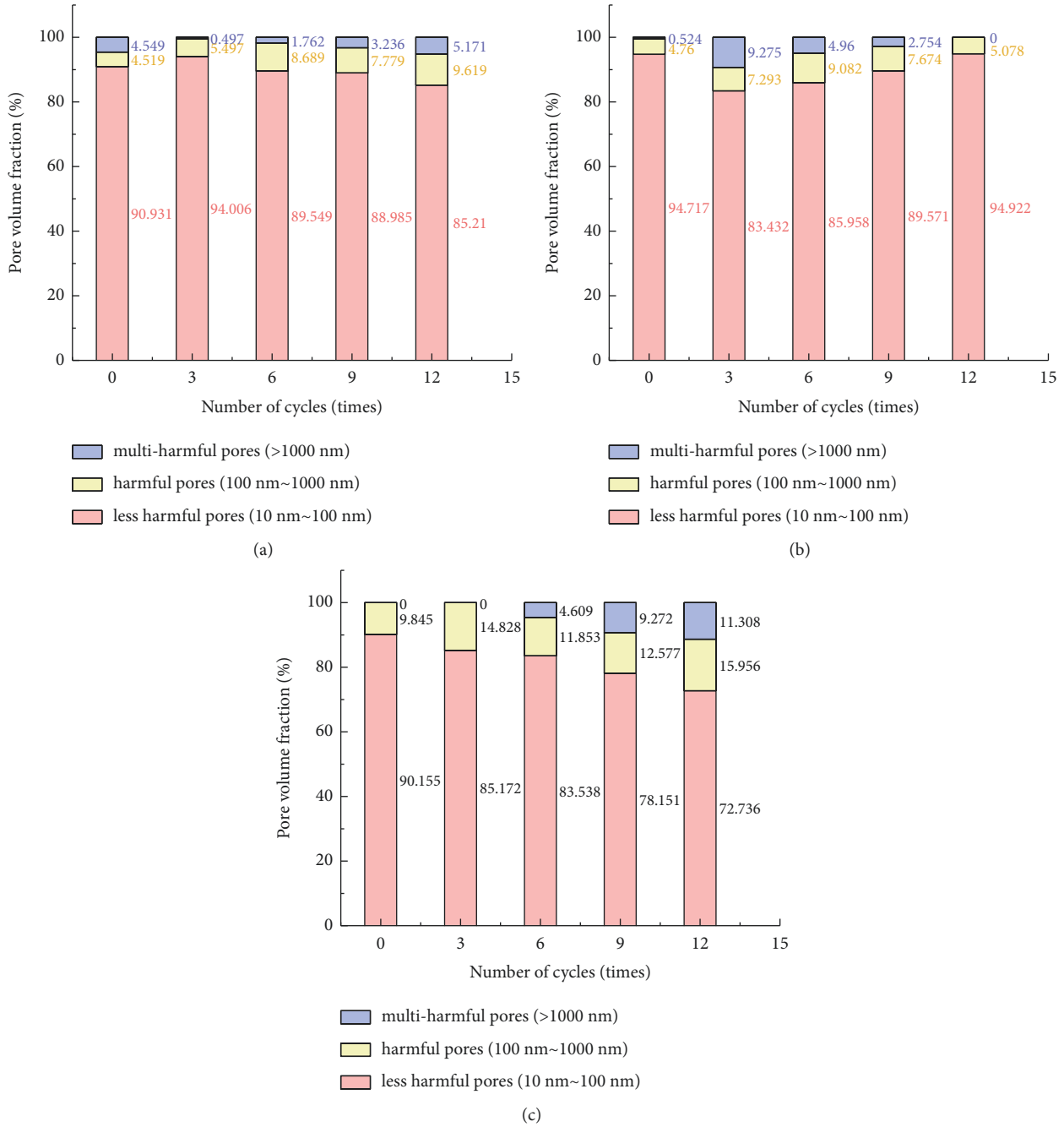

Figure 10: Pore volume fraction distribution of semirigid base material under different cycle times. (a) 20°C~60°C. (b) −5°C~−30°C. (c) −20°C~20°C.

Table 11: NMR spectral area of semirigid base after different number of cycles at different temperature intervals.

Temperature intervals (°C)	Number of cycles (times)	Total area of T2 spectrum (cm^2)	Less harmful hole area (cm^2)	Harmful hole area (cm^2)	More harmful hole area (cm^2)
20~60	0	905.89	823.738	40.939	41.213
	3	360.64	339.023	19.824	1.793
	6	1403.905	1257.177	121.987	24.742
	9	858.835	764.234	66.805	27.796
	12	390.767	332.972	37.589	20.207
−5~−30	0	1029.081	974.708	48.98	5.393
	3	895.551	747.175	65.314	83.062
	6	890.148	765.157	80.847	44.144
	9	872.389	781.408	66.951	24.03
	12	501.842	476.357	25.485	0
−20~20	0	894.658	806.581	88.077	0
	3	1027.467	875.112	152.354	0
	6	869.981	726.762	103.12	40.099
	9	1292.425	1010.037	162.551	119.837
	12	1305.531	949.593	208.309	11.308

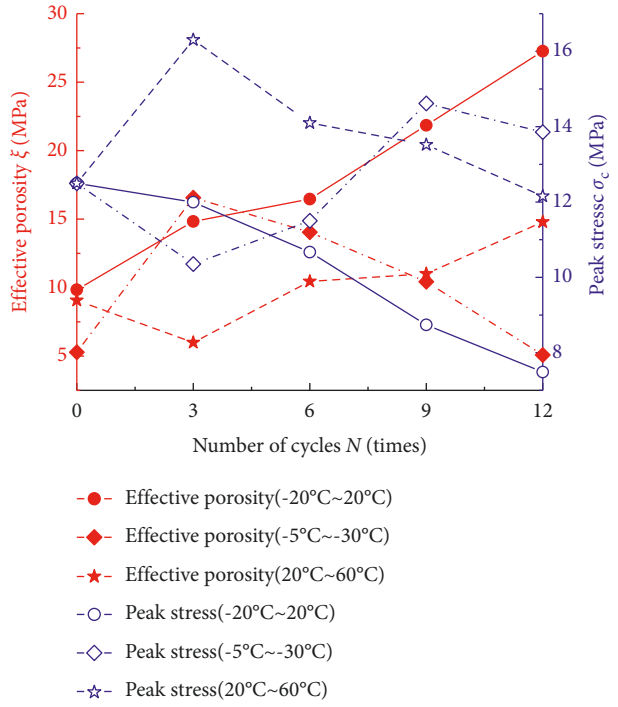

Figure 11: Peak stress and effective porosity after different number of cycles.

sizes; thus, it can visually reflect the changes of the internal structure of the pores [47], and the NMR spectral areas of the semirigid base after different number of cycles at different temperature intervals are detailed in Table 11. The percentage of T_2 spectral area of different pore classes (less harmful pores, harmful pores, and more harmful pores) to the total T_2 spectral area is approximated as the pore volume fraction, as shown in Figure 10. Combined with the analysis in Table 11 and Figure 10, it can be seen that, regardless of the environment, the percentage of the number of less harmful pores far exceeds the percentage of the number of harmful pores and the percentage of the number of more harmful pores. The freeze-thaw environment damages the material more deeply, resulting in a significantly higher percentage of harmful pore counts and more harmful pore counts than those in high- and low-temperature environments. Specifically, the percentage of harmful pores and multiple harmful pores under freeze-thaw environment varied with the number of cycles as 9.85%, 14.83%, 11.85%, 12.58%, 15.96%, 0.00%, 0.00%, 4.61%, 9.27%, and 11.31%, respectively. The percentage of harmful pores and multi-harmful pores under high-temperature environment varied with the number of cycles as 4.52%, 5.50%, 8.69%, 7.78%, 9.62%, 4.55%, 0.50%, 1.76%, 3.24%, and 5.17%, respectively.

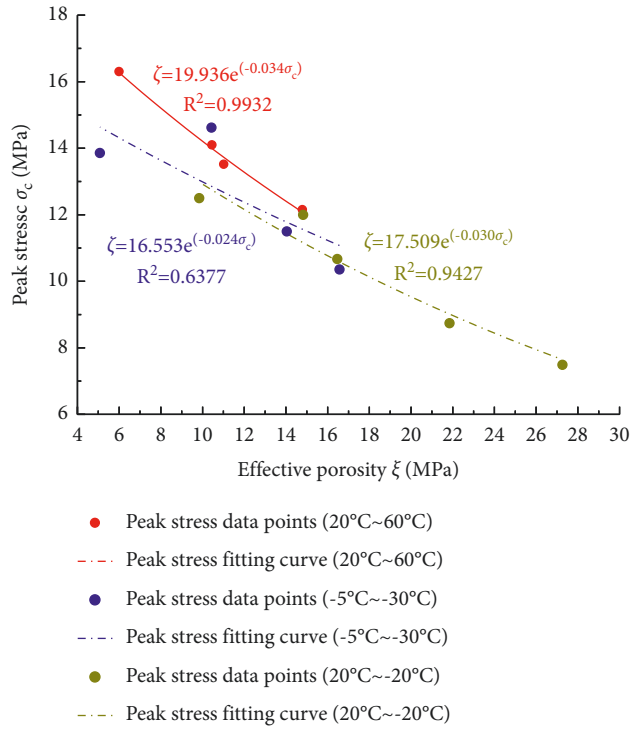

Figure 12: Relationship between pore efficiency and peak stress at different temperature intervals.

The percentage of harmful pores and multiharmful pores varied with the number of cycles in low-temperature environment as 4.76%, 7.29%, 9.08%, 7.67%, 5.08%, 0.52%, 9.36%, 4.96%, 2.75%, and 0.00%, respectively.

Based on the above analysis, this paper defines the sum of the percentage of harmful pores and the percentage of multiple harmful pores as the effective porosity of the semirigid base material ξ. This paper describes the evolution of mechanical properties of semirigid base material after different cycles under different environments based on the change of pore content (Figure 11) so as to analyze the macrofine scale linkage of damage characteristics of semirigid base material under large temperature difference conditions and provide relevant data support and reference value for the subsequent study of this kind of pavement engineering problems. According to the test results, the relationship curve between the effective porosity of NMR and peak stress was established, as shown in Figure 12. Combining Figures 11 and 12, it can be seen that the peak stress is negatively correlated with the change of effective porosity as the number of cycles increases, and the effective porosity shows a decreasing trend with the number of cycles at low temperatures, and vice versa at high-temperature and freeze-thaw environments. It is shown that the mechanical properties of semirigid base material under freeze-thaw and high-temperature environments decrease exponentially as a function of the increase in effective porosity, while the mechanical properties of semirigid base material under low-temperature environments increase exponentially as a function of the decrease in effective porosity. This is more consistent with the results of Zhang et al. [23,48].

4. Conclusions

The variation patterns of peak stress and dynamic modulus of semirigid base materials under different temperature intervals show significant variability. The freeze-thaw environment shows an overall deterioration of the peak stress of the material, and the dynamic modulus damage temperature damage influence factor is as high as 0.67~0.77. The effect of freeze-thaw environment is the most significant.

In a high-temperature environment, peak stress and dynamic modulus show a power function and polynomial functions, respectively, with respect to the number of cycles. In a low-temperature environment, the peak stress, dynamic modulus, and the number of cycles show polynomial functions. In the freeze-thaw environment, both peak stress and dynamic modulus show a power function with respect to the number of cycles. There is a significant correlation between the axial load resistance and deformation resistance of semirigid base material under freeze-thaw and low-temperature environments.

The differences in damage characteristics of the semirigid base under different environments are mainly reflected in the dynamic evolution of pore structure and pore size, which are rooted in the differences in the expansion and contraction characteristics of each microscopic phase of the material and the differences in the mechanical interface effects on the internal pores, but the macroscopic damage mode is mainly based on tensile damage. The peak stress and effective porosity of the semirigid base under different environments are exponentially related.

Data Availability

The data used to support the findings of this study are available from the corresponding author upon request.

Conflicts of Interest

The funders had no role in the design of the study; in the collection, analyses, or interpretation of data; in the writing of the manuscript; or in the decision to publish the results. Moreover, The authors declare that there are no conflicts of interest regarding the publication of this paper.

Authors' Contributions

Jia Pan and Yanjun Shen carried out the figure preparation, analysis, manuscript preparation, and editing. Ming Dai planned and designed the research. Jianbo Deng conducted the study. Yeermulati Muhadeer performed the data collection.

Acknowledgments

This research was supported by the National Natural Science Foundation of China (Grant no. 41772333), the Foundation of Shaanxi Key Laboratory of Safety and Durability of Concrete Structures, Xijing University (Grant no. XJKFJJ201802), and Yulin 2020 Science and Technology Plan (Industry University Research) Project (CXY-2020-034).

References

[1] A. Toktorbai uulu, H. Katsuchi, H. Kim, H. Yamada, and Y. Ijima, "Study on thermal parameters of asphalt concrete for countermeasures against high surface temperature of pavement in tunnel," *Road Materials and Pavement Design*, vol. 22, no. 4, pp. 954–968, 2021.

[2] Y. Zhao, J. Jiang, Y. Dai, L. Zhou, and F. Ni, "Thermal property evaluation of porous asphalt concrete based on heterogeneous meso-structure finite element simulation," *Applied Science-Basel*, vol. 10, no. 5, p. 1671, 2020.

[3] X. Wang, K. Li, Y. Zhong, Q. Xu, and C. Li, "XFEM simulation of reflective crack in asphalt pavement structure under cyclic temperature," *Construction and Building Materials*, vol. 189, pp. 1035–1044, 2018.

[4] M. He, S. Ma, C. Liu, J. Zhang, and S. Yuan, "Effect of microcracking on the shrinkage cracking and durability performance of cement-treated macadam material," *International Journal of Pavement Engineering*, vol. 2021, pp. 1–14, 2021.

[5] Y. Wang, Y. Tan, M. Guo, Z. Liu, and X. Wang, "Study on the dynamic compressive resilient modulus and frost resistance of semi-rigid base materials," *Road Materials and Pavement Design*, vol. 18, no. 3, pp. 259–269, 2017.

[6] J. Li, F. Wang, F. Yi, J Ma, and Z Lin, "Fractal analysis of the fracture evolution of freeze-thaw damage to asphalt concrete," *Materials*, vol. 12, no. 14, p. 2288, 2019.

[7] F. Xu, M. Zhou, J. Chen, and S. Ruan, "Mechanical performance evaluation of polyester fiber and SBR latex compound-modified cement concrete road overlay material," *Construction and Building Materials*, vol. 63, pp. 142–149, 2014.

[8] B. Doll, H. Ozer, J. Rivera-Perez, I. L. Al-Qadi, and J. Lambros, "Damage zone development in heterogeneous asphalt concrete," *Engineering Fracture Mechanics*, vol. 182, pp. 356–371, 2017.

[9] S. Li, G. Wu, and H. Shi, "Acoustic emission characteristics of semi-rigid bases with three moisture conditions during bending tests," *Road Materials and Pavement Design*, vol. 20, no. 1, pp. 187–198, 2019.

[10] J. Hu, Z. Qian, P. Liu, D. Wang, and M. Oeser, "Investigation on the permeability of porous asphalt concrete based on microstructure analysis," *International Journal of Pavement Engineering*, vol. 21, no. 13, pp. 1683–1693, 2020.

[11] Y. Zhao, X. Wang, J. Jiang, and L. Zhou, "Characterization of interconnectivity, size distribution and uniformity of air voids in porous asphalt concrete using X-ray CT scanning images," *Construction and Building Materials*, vol. 213, pp. 182–193, 2019.

[12] C. Liang, Y. Wang, G. Tan, L. Zhang, Y. Zhang, and Z. Yu, "Analysis of internal structure of cement-stabilized macadam based on industrial CT scanning," *Advances in Materials Science and Engineering*, vol. 2020, Article ID 5265243, 2020.

[13] W.-x. Zheng, X.-y. Xiao, C.-g. Chang et al., "Characterizing properties of magnesium oxychloride cement concrete pavement," *Journal of Central South University*, vol. 26, no. 12, pp. 3410–3419, 2019.

[14] A. Pandey and B. Kumar, "Effects of rice straw ash and micro silica on mechanical properties of pavement quality concrete," *Journal of Building Engineering*, vol. 26, Article ID 100889, 2019.

[15] J. Liu, B. Yu, and Q. Wang, "Application of steel slag in cement treated aggregate base course," *Journal of Cleaner Production*, vol. 269, Article ID 121733, 2020.

[16] N. Hasheminejad, C. Vuye, A. Margaritis et al., "Investigation of crack propagation and healing of asphalt concrete using digital image correlation," *Applied Science-Basel*, vol. 9, no. 12, p. 2459, 2019.

[17] B. Behnia, W. Buttlar, and H. Reis, "Evaluation of low-temperature cracking performance of asphalt pavements using acoustic emission: a review," *Applied Sciences*, vol. 8, no. 2, p. 306, 2018.

[18] Y. Tan, Z. Sun, X. Gong, H. Xu, L. Zhang, and Y. Bi, "Design parameter of low-temperature performance for asphalt mixtures in cold regions," *Construction and Building Materials*, vol. 155, pp. 1179–1187, 2017.

[19] H. Liu, W. Li, G. Luo, S Liu, and X Lyu, "Mechanical properties and fracture behavior of crumb rubber basalt fiber concrete based on acoustic emission technology," *Sensors*, vol. 20, no. 12, 2020.

[20] H. Wei, B. Hu, F. Wang, J. Zheng, J. Jin, and C. Liu, "Temporal-spatial evolution characteristics of acoustic emission in asphalt concrete cracking process under low temperature," *Construction and Building Materials*, p. 248, 2020.

[21] L. Gao, F. Ni, C. Ling, and J. Yan, "Evaluation of fatigue behavior in cold recycled mixture using digital image correlation method," *Construction and Building Materials*, vol. 102, no. 1, pp. 393–402, 2016.

[22] B. Bai, R. Zhou, G. Cai, W. Hu, and G. Yang, "Coupled thermo-hydro-mechanical mechanism in view of the soil particle rearrangement of granular thermodynamics," *Computers and Geotechnics*, vol. 137, no. 8, Article ID 104272, 2021.

[23] K. Zhang, J. Zhou, and Z. Yin, "Experimental study on mechanical properties and pore structure deterioration of

concrete under freeze-thaw cycles," *Materials*, vol. 14, no. 21, 2021.

[24] J. Li, R. B. Kaunda, and K. Zhou, "Experimental investigations on the effects of ambient freeze-thaw cycling on dynamic properties and rock pore structure deterioration of sandstone," *Cold Regions Science and Technology*, vol. 154, pp. 133–141, 2018.

[25] I. Menapace, L. Garcia Cucalon, F. Kaseer, E. Masad, and A. Epps Martin, "Application of low field nuclear magnetic resonance to evaluate asphalt binder viscosity in recycled mixes," *Construction and Building Materials*, vol. 170, pp. 725–736, 2018.

[26] I. Menapace, E. Masad, G. Papavassiliou, and E. Kassem, "Evaluation of ageing in asphalt cores using low-field nuclear magnetic resonance," *International Journal of Pavement Engineering*, vol. 17, no. 10, pp. 847–860, 2016.

[27] Y. Zhang, X. Liu, Y. Xu, B. Tang, Y. Wang, and E. Mukiza, "Preparation and characterization of cement treated road base material utilizing electrolytic manganese residue," *Journal of Cleaner Production*, vol. 232, pp. 980–992, 2019.

[28] Y. Zhang, X. Liu, Y. Xu, B. Tang, Y. Wang, and E. Mukiza, "Synergic effects of electrolytic manganese residue-red mud-carbide slag on the road base strength and durability properties," *Construction and Building Materials*, vol. 220, pp. 364–374, 2019.

[29] L. M. Nicula, O. Corbu, I. Ardelean, A. V Sandu, M Iliescu, and D Simedru, "Freeze-thaw effect on road concrete containing blast furnace slag: NMR relaxometry investigations," *Materials*, vol. 14, no. 12, 2021.

[30] D. R. Biswal, U. C. Sahoo, and S. R. Dash, "Non-destructive strength and stiffness evaluation of cement-stabilised granular lateritic soils," *Road Materials and Pavement Design*, vol. 21, no. 3, pp. 835–849, 2020.

[31] X. Sun, S. Wu, J. Yang, and R. Yang, "Mechanical properties and crack resistance of crumb rubber modified cement-stabilized macadam," *Construction and Building Materials*, vol. 259, Article ID 119708, 2020.

[32] B. Bai, Q. Nie, Y. Zhang, X. Wang, and W. Hu, "Cotransport of heavy metals and SiO2 particles at different temperatures by seepage," *Journal of Hydrology*, vol. 597, Article ID 125771, 2021.

[33] Y. Zhao, X. Yang, Q. Zhang, N. Liang, Y. Xiang, and M. Qin, "Crack resistance and mechanical properties of polyvinyl alcohol fiber-reinforced cement-stabilized macadam base," *Advances in Civil Engineering*, vol. 2020, Article ID 6564076, 15 pages, 2020.

[34] X. Yan, L. Chen, Q. You, and Q. Fu, "Experimental analysis of thermal conductivity of semi-rigid base asphalt pavement," *Road Materials and Pavement Design*, vol. 20, no. 5, pp. 1215–1227, 2019.

[35] D. R. Biswal, U. C. Sahoo, and S. R. Dash, "Characterization of granular lateritic soils as pavement material," *Transportation Geotechnics*, vol. 6, pp. 108–122, 2016.

[36] S. Lv, C. Xia, H. Liu et al., "Strength and fatigue performance for cement-treated aggregate base materials," *International Journal of Pavement Engineering*, vol. 22, no. 6, pp. 690–699, 2021.

[37] T.-h. Wang, L.-j. Su, and J.-y. Zhai, "A case study on diurnal and seasonal variation in pavement temperature," *International Journal of Pavement Engineering*, vol. 15, no. 5, pp. 402–408, 2014.

[38] B. Zhang, X. Zhang, Y. Zhong, X. Li, M. Hao, and J. Liu, "Dynamic inversion analysis of structural layer modulus of semirigid base pavement considering the influence of temperature and humidity," *Advances in Civil Engineering*, vol. 2020, pp. 1–12, 2020.

[39] A. Moghadam, N. B. Harris, K. Ayranci, J. S. Gomez, N. A. Angulo, and R. Chalaturnyk, "Brittleness in the devonian horn river shale, british columbia, Canada," *Journal of Natural Gas Science and Engineering*, vol. 62, pp. 247–258, 2019.

[40] I. Barisic, S. Dimter, and T. Rukavina, "Elastic properties of cement-stabilised mixes with steel slag," *International Journal of Pavement Engineering*, vol. 17, no. 9, pp. 753–762, 2016.

[41] Z. Rong-rong and M. Dong-dong, "Effects of curing time on the mechanical property and microstructure characteristics of metakaolin-based geopolymer cement-stabilized silty clay," *Advances in Materials Science and Engineering*, vol. 2020, Article ID 9605941, 9 pages, 2020.

[42] T. M. AlGhamdi, C. H. H. Arns, and R. Y. Y. Eyvazzadeh, "Correlations between NMR-relaxation response and relative permeability from tomographic reservoir-rock images," *SPE Reservoir Evaluation and Engineering*, vol. 16, no. 4, pp. 369–377, 2013.

[43] L. Liu, Z. He, X. Cai, and S. Fu, "Application of low-field NMR to the pore structure of concrete," *Applied Magnetic Resonance*, vol. 52, no. 1, pp. 15–31, 2021.

[44] G. Turuallo and M. N. Soutsos, "Supplementary cementitious materials: strength development of self-compacting concrete under different curing temperature," *Procedia Engineering*, vol. 125, pp. 699–704, 2015.

[45] T. J. MacLean and A. Lloyd, "Compressive stress-strain response of concrete exposed to low temperatures," *Journal of Cold Regions Engineering*, vol. 33, no. 4, 2019.

[46] B. Zhang, B. Wang, Y. Zhong, X. Li, Y. Zhang, and S. Li, "Damage characteristics and microstructures of low-exothermic polymer grouting materials under F-T cycles," *Construction and Building Materials*, vol. 294, Article ID 123390, 2021.

[47] X. Wang, X. Shen, H. Wang, C. Gao, and T. Zhang, "Nuclear magnetic resonance analysis of freeze-thaw damage in natural pumice concrete," *Materials DE Construction*, vol. 66, no. 322, 2016.

[48] R. Kumar and B. Bhattacharjee, "Porosity, pore size distribution and in situ strength of concrete," *Cement and Concrete Research*, vol. 33, no. 1, pp. 155–164, 2003.